

# $\alpha$ -Helices direct excitation energy flow in the Fenna–Matthews–Olson protein

Frank Müh<sup>†‡</sup>, Mohamed El-Amine Madjet<sup>†</sup>, Julia Adolphs<sup>†</sup>, Ayjama Abdurahman<sup>†§</sup>, Björn Rabenstein<sup>†</sup>, Hiroshi Ishikita<sup>†¶</sup>, Ernst-Walter Knapp<sup>†</sup>, and Thomas Renger<sup>†‡</sup>

<sup>†</sup>Institute for Chemistry and Biochemistry (Crystallography), Free University of Berlin, Takustrasse 6, 14195 Berlin, Germany; <sup>§</sup>Department of Physics, Xinjiang University, Urumqi 830046, China; and <sup>¶</sup>Department of Chemistry, University of Southern California, Los Angeles, CA 90089

Communicated by Rudolph A. Marcus, California Institute of Technology, Pasadena, CA, August 30, 2007 (received for review April 13, 2007)

In photosynthesis, light is captured by antenna proteins. These proteins transfer the excitation energy with almost 100% quantum efficiency to the reaction centers, where charge separation takes place. The time scale and pathways of this transfer are controlled by the protein scaffold, which holds the pigments at optimal geometry and tunes their excitation energies (site energies). The detailed understanding of the tuning of site energies by the protein has been an unsolved problem since the first high-resolution crystal structure of a light-harvesting antenna appeared >30 years ago [Fenna RE, Matthews BW (1975) *Nature* 258:573–577]. Here, we present a combined quantum chemical/electrostatic approach to compute site energies that considers the whole protein in atomic detail and provides the missing link between crystallography and spectroscopy. The calculation of site energies of the Fenna–Matthews–Olson protein results in optical spectra that are in quantitative agreement with experiment and reveals an unexpectedly strong influence of the backbone of two  $\alpha$ -helices. The electric field from the latter defines the direction of excitation energy flow in the Fenna–Matthews–Olson protein, whereas the effects of amino acid side chains, hitherto thought to be crucial, largely compensate each other. This result challenges the current view of how energy flow is regulated in pigment–protein complexes and demonstrates that attention has to be paid to the backbone architecture.

energy transfer | light-harvesting | optical spectra | photosynthesis | structure-based simulation

Photosynthesis is the fundamental biological process in which solar energy is converted into biomass. The first step is the capture of light by arrays of protein-bound dye molecules (pigments). These pigment–protein complexes (PPCs) are therefore termed light-harvesting complexes or antenna proteins (1). They transfer the excitation energy with high quantum yield to specialized PPCs, the reaction centers, where the energy is used to trigger the chemical modification of substrates. To guide the excitation energy flow in a certain direction there has to be an energy sink, that is, the pigments in the target region are required to absorb at lower energies than the initially excited chromophores. A complication of this simple picture arises from long-range electrostatic interactions between the local excitations (excitonic couplings), which are a prerequisite for energy transfer. These couplings cause the excited states of the PPC (exciton states) to be delocalized, that is, their electronic wave functions contain contributions of several pigments in the complex. Directed energy transport results from energetic relaxation transferring population between exciton states of different spatial extents. The latter depend crucially on excitonic couplings and site energies, so that the elucidation of energy-transfer mechanisms on the basis of spectroscopic data (2–4) and crystal structures (5–7) requires knowledge of both these quantities (8, 9), which are not directly available from experiments.

Whereas there are various methods at different levels of approximation to accurately determine excitonic couplings from structural data (10–15), the calculation of site energies has been

a challenge (15–17). In earlier attempts to calculate site energies directly by using the information from crystal structures, quantum chemical methods were applied to the pigment cofactors and their immediate protein environment (16, 17). A shortcoming of a solely quantum chemical method is that important long-range electrostatic pigment–protein couplings are not taken into account. Recently, we considered the effects of charged amino acid residues in a very simple model (15). In this model, a standard protonation state of titratable groups is assumed (corresponding to pH 7, 300 K in water), and the difference,  $\Delta\Phi = \Phi_1 - \Phi_0$ , of the electrostatic potential of the pigment molecule between its first excited ( $S_1$ ) and its ground state ( $S_0$ ), which is crucial for the understanding of site energy shifts (see below), is approximated by the potential of a dipole. Although not restricted to the immediate protein environment of pigments, this approach yields only part of the answer to the site energy problem, because the charge density in the neutral protein environment of the pigments is neglected and the dipole approximation of  $\Delta\Phi$  is too simple for short-range interactions with the protein. In particular, hydrogen bond effects are not described correctly.

Here, we present a method that emphasizes the role of detailed charge distributions of both the pigment states and the protein. We combine the quantum chemistry of pigments with classical electrostatic calculations of the whole PPC in atomic detail. The method aims at a realistic description of the internal electric field experienced by individual pigments in the PPC, giving rise to specific site energy shifts. The electric field originates from neutral and charged amino acid side chains, the peptide backbone, other cofactors, as well as the polarization of the protein dielectric volume and the surrounding solvent or glass. Our simulations take into account all these aspects, allowing us to unravel in detail the various contributions to site energy differences on the basis of a crystal structure. In addition, we consider conformational differences between pigments and the consequences of nonstandard protonation patterns resulting from protein- and environment-induced changes of acid–base equilibria of titratable residues (18–20). In the classical electrostatic part of the simulations, we calculate the free energy change of the PPC that occurs when the charge density of a pigment in its  $S_0$  state is changed into that of the  $S_1$  state, taking into account the nonequilibrium polarization (21) of the dielectric medium after optical excitation [see *Computational Procedures* and [supporting information \(SI\) Text](#)].

Author contributions: T.R. designed research; F.M., M.E.M., J.A., A.A., and T.R. performed research; B.R., H.I., and E.-W.K. contributed new analytic tools; F.M. analyzed data; and F.M. and T.R. wrote the paper.

The authors declare no conflict of interest.

Abbreviations: BChl<sub>a</sub>, bacteriochlorophyll *a*; FMO, Fenna–Matthews–Olson protein; PPC, pigment–protein complex.

<sup>†</sup>To whom correspondence may be addressed. E-mail: mueh@chemie.fu-berlin.de or rth@chemie.fu-berlin.de.

This article contains supporting information online at [www.pnas.org/cgi/content/full/0708222104/DC1](http://www.pnas.org/cgi/content/full/0708222104/DC1).

© 2007 by The National Academy of Sciences of the USA

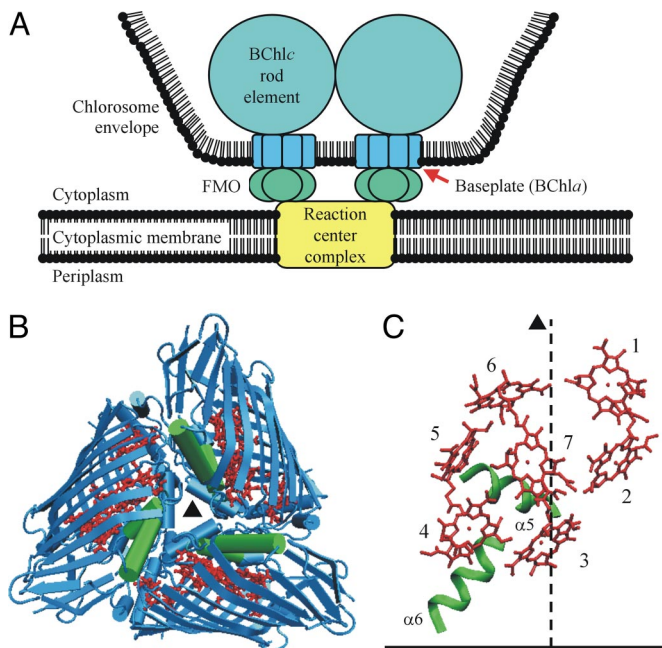


**Fig. 1.** Structure of the FMO protein. (A) Schematic representation of the location of the FMO protein in the photosynthetic apparatus of green sulfur bacteria according to the most recent models (23, 24). (B) Ribbon diagram of the FMO trimer with the  $C_3$ -symmetry axis ( $\blacktriangle$ ) perpendicular to the paper plane [backbone, blue;  $\alpha$ -helices 5 and 6, green; BChla, red; Protein Data Bank (PDB) ID code 4BCL]. (C) Arrangement of BChla pigments (red) and  $\alpha$ -helices 5 and 6 (green) in one FMO monomer with their proposed (15) orientation relative to the cytoplasmic membrane (horizontal bar). The dashed line indicates the orientation of the  $C_3$  axis. The two  $\alpha$ -helices 5 and 6 create an energy sink at BChla 3 as explained in the text and in Fig. 3.

We applied our method to the Fenna–Matthews–Olson (FMO) protein of green sulfur bacteria (1, 22). Under physiological conditions, this water-soluble PPC is situated between the so-called baseplate protein of the major antenna system of green sulfur bacteria, the chlorosomes (23, 24), and the reaction center complex (25, 26). Here, it mediates excitation energy transfer from the bacteriochlorophyll *c* rods to the reaction center pigments (Fig. 1A). The FMO protein consists of a  $C_3$ -symmetric trimer (Fig. 1B). Each monomer forms a pocket made of antiparallel  $\beta$ -sheets that encloses a core of seven bacteriochlorophyll *a* (BChla) cofactors (Fig. 1C) and is capped on one side by several  $\alpha$ -helical segments (Fig. 1B and C; SI Fig. 5) (6, 7). Because the FMO protein is the first PPC for which a high-resolution crystal structure (1.9 Å) became available (5, 6), it has been used for many years to explore structure–function relationships in antenna proteins. A major step toward a structure-based understanding of the optical spectra  $\approx 12,500\text{ cm}^{-1}$  (800 nm,  $Q_Y$  region of BChla) was taken recently by the assumption (2, 27) and quantitative explanation (15) of a rather small effective dipole strength of the  $Q_Y$  transitions of the BChla pigments resulting from dielectric screening and local field effects. The correspondingly decreased excitonic couplings allowed for a better simulation of spectra by using site energies as free fit parameters, but the full assignment of site energies on the basis of the crystal structure remained an unsolved problem.

## Results and Discussion

Simulated absorption, circular dichroism, and linear dichroism spectra at 4 K of the FMO trimer from *Prosthecochloris aestuarii* are compared in Fig. 2A with experimental data (2). Each exciton state leads to a band in the absorption spectrum, the position and intensity of which are determined by the calculated

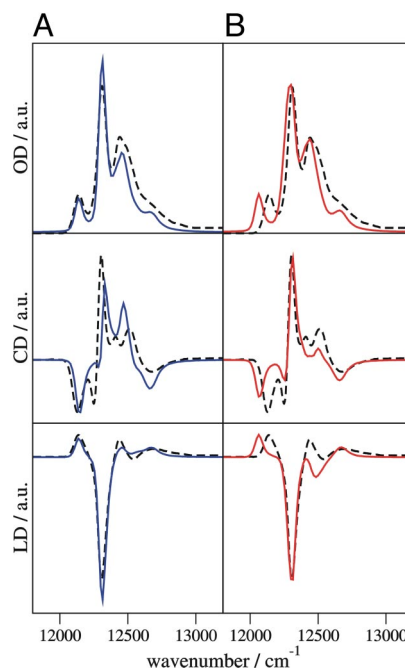


**Fig. 2.** Simulated optical absorption (OD), circular dichroism (CD), and linear dichroism (LD) spectra of the FMO trimer, using site energies from structure-based calculations (blue and red lines), compared with experimental results (2) (dashed lines). a.u., arbitrary units. (A) Nonstandard protonation pattern at 4 K (blue). (B) Standard protonation pattern. All Asp and Glu are negatively charged and all Arg and Lys are positively charged (red).

site energies and excitonic couplings. The shape of the bands is simulated by taking into account the modulation of site energies by the vibrations of the PPC (8, 9). The agreement between simulated and measured spectra in Fig. 2A is excellent considering that practically no adjustable parameters are used. All features of the experimental spectra are recovered, in particular, a separated band on the low-energy side of the spectrum representing the energy sink. The calculated site energies (SI Table 1) and earlier fitting results (2, 15) correlate well (SI Fig. 6). This correlation suggests that the error of site energies calculated by the combined quantum chemical/electrostatic method is in the order of  $60\text{ cm}^{-1}$ .

In contrast to fitting procedures, the present approach allows one to relate site energies to details of the crystal structure. By setting selected parts of the charge density to zero in the calculations, it is possible to elucidate the role of different regions of the protein. Rather unexpectedly, the largest influence on a site energy, contributing a shift of about  $-300\text{ cm}^{-1}$ , originates from the peptide backbone of  $\alpha$ -helices 5 and 6 (Figs. 1 and 3; SI Fig. 5, SI Tables 1–3). This effect causes BChla 3 to have by far the lowest site energy. Single amino acid side chains, either charged or neutral, cause shift magnitudes of at most  $\approx 180\text{ cm}^{-1}$  and tend to compensate each other (SI Tables 3–5). Accordingly, the charged amino acids do not play the dominant role that was attributed to them in earlier studies (15–17, 28), where large parts of the protein charge distribution, in particular, the backbone, were not modeled, and standard protonation states of titratable residues were assumed (15–17). In qualitative agreement with experimental results on other antenna systems (29), hydrogen bond donors to BChla cause red shifts of the site energies, but in the present system this shift never exceeds  $\approx 130\text{ cm}^{-1}$  (SI Table 4).

The BChla cofactors in the seven sites have slightly different conformations. In particular, they differ in the orientation of the 3-acetyl group at ring A and the out-of-plane distances of the

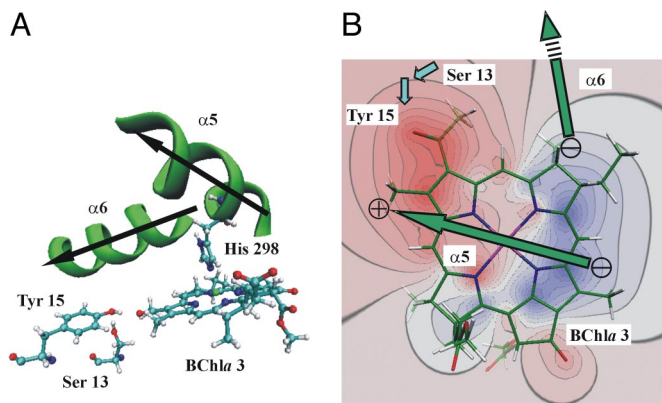


**Fig. 3.** Pigment-protein interactions of the energy sink (BChla 3) in the FMO protein that were modified in the simulations shown in Fig. 4. (A) Arrangement of  $\alpha$ -helices 5 (including the axial ligand His-298) and 6, as well as residues Ser-13 and Tyr-15 relative to BChla 3. The arrows indicate the helix dipoles pointing from the C to the N terminus. (B) Contour plot of the difference  $\Delta\Phi$  of the *ab initio* electrostatic potential of BChla 3 between the  $S_1$  and  $S_0$  states in the plane of the tetrapyrrole macrocycle (blue,  $\Delta\Phi > 0$ ; red,  $\Delta\Phi < 0$ ). The green arrows indicate the location of the dipoles of  $\alpha$ -helices 5 and 6 above the plane with the  $\oplus$  and  $\ominus$  signs representing the effective partial charges (31, 32). The blue arrows indicate the positions of the hydroxyl group dipoles of Ser-13 and Tyr-15, where the latter is located approximately in the plane and the former is below the plane.

conjugated atoms in the tetrapyrrole macrocycle (6). These conformational variations are explicitly taken into account in the electrostatic calculations by assigning partial charges to atomic positions based on the crystal structure. In the quantum chemical calculations, which produce conformation-dependent atomic partial charges and vacuum site energy shifts ( $\Delta X_{qc}^{(m)}$  in Eq. 1), we only consider the different acetyl group orientations. The comparison between simulated and measured spectra suggests that the neglect of the out-of-plane bending in the quantum chemical part produces no severe errors. In fact, we conclude that the contribution of the structural distortions to site energy differences is below  $100 \text{ cm}^{-1}$  and hence significantly smaller than suggested in earlier work (16). We do not exclude, however, the possibility that the nonplanarity of the macrocycles contributes to an overall red shift of the site energies with respect to the absorption of BChla in organic solvents.

The calculation of protonation probabilities reveals a single pattern at 4 K, where 49% of the acidic and basic side chains are neutral, that is, they deviate from their standard protonation state. This high percentage of neutral groups is a consequence of the low dielectric constant of  $\epsilon_{\text{solv}} = 10$  assigned to the water/glycerol mixture below the glass transition temperature (30), which results in a destabilization of solvent-exposed, charged groups. Calculating with  $\epsilon_{\text{solv}} = 80$  (corresponding to liquid water) results in 11% of the titratable groups being in their nonstandard protonation state. The site energies obtained under these more physiological conditions deviate by maximally  $72 \text{ cm}^{-1}$  from those with  $\epsilon_{\text{solv}} = 10$  (SI Table 6). This result suggests that site energies can be temperature-dependent because of a change in the protonation pattern resulting from a variation of the solvent dielectric constant around the glass transition temperature. The site energy changes are close to the estimated error of the calculations, however, and are smaller than the measured optical linewidth at higher temperatures. Thus, we consider the site energies of the FMO protein as practically temperature-independent. Changes of site energies of up to  $135 \text{ cm}^{-1}$  (SI Table 6) are obtained if a standard protonation pattern is assumed as in earlier work (15–17), where all acids and bases are fully charged. The resulting simulated spectra are still close

to experiment (Fig. 2B). The calculated circular dichroism spectrum seems to describe the experimental data even slightly better, but the overall agreement with all three measured spectra is weaker because of the incorrect protonation pattern.

An illustration of the main mechanism that creates the energy sink in the FMO protein at BChla 3 is given in Fig. 3B, where the difference  $\Delta\Phi$  between the electrostatic potentials of the  $S_1$  and  $S_0$  states of this pigment is shown together with the backbone dipole moments of  $\alpha$ -helices 5 and 6. If a positive charge is placed in the positive or negative regions of  $\Delta\Phi$ , the site energy is shifted to higher or lower energies, respectively, and vice versa for a negative charge. In an  $\alpha$ -helix, the arrangement of peptide bonds gives rise to an electrostatic potential that is essentially that of an extended dipole formed by two partial charges of opposite signs placed at the ends of the helix (31, 32). In the FMO protein,  $\alpha$ -helix 5 is positioned close to BChla 3 such that its positive end (head of green arrow in Fig. 3B) lies in the region of negative  $\Delta\Phi$  and its negative end lies in the region of positive  $\Delta\Phi$ , which results in a strong red shift of the site energy ( $-200 \text{ cm}^{-1}$ ). Whereas  $\alpha$ -helix 5 seems to be optimized to fit into the difference potential of BChla 3,  $\alpha$ -helix 6 points away from this pigment and therefore causes a less pronounced red shift ( $-100 \text{ cm}^{-1}$ ). The magnitude of the effective partial charges representing an  $\alpha$ -helix dipole was estimated to be  $0.5\text{--}0.75 e$  (31, 32) in good agreement with our estimates. Hence, the effect of the end of an  $\alpha$ -helix is similar to that of a charged amino acid side chain but is independent of protonation states.

To study the control of excitation energy flow by the  $\alpha$ -helices 5 and 6 under physiological conditions, we simulated exciton relaxation dynamics at 300 K in the native FMO protein (Fig. 4 Left) and in two modified systems. In one case, the backbone partial charges of the two helices were set to zero (Fig. 4 Center). In the other case, we investigated a double mutant to assess the influence of hydrogen bonding to the 3-acetyl group of BChla 3 (Fig. 4 Right). In this mutant, the OH-dipoles of Ser-13 and Tyr-15 (Fig. 3) were removed by replacing the charge distributions of these two residues with those of Ala and Phe, respectively, which do not form hydrogen bonds. Following our earlier proposal (15), we assume that the FMO protein is oriented with BChla 1 and 6 toward the baseplate, whereas BChla 3 and 4 define the target region facing the reaction center complex (Fig. 1 A and C). Accordingly, the initial probability of being excited is highest for those exciton states that have large contributions from BChla 1 and 6 (Fig. 4; SI Figs. 7 and 8). The native system equilibrates within 2 ps such that 50% of the excitation is located at BChla 3 and 4 (Fig. 4 Left; SI Fig. 8). This result illustrates how exciton relaxation leads to a spatially directed energy transport. When the backbone partial charges of  $\alpha$ -helices 5 and 6 are set to zero, BChla 3 and 4 end up with only 20% excitation (Fig. 4 Center; SI Fig. 8). The restriction of energy flow in the modified system is caused by the removal of the energy sink at BChla 3 as seen from the disappearance of the low-energy band in the simulated absorption spectrum. In the double mutant, there is still net energy transfer with 40% excitation being finally found on BChla 3 and 4 (Fig. 4 Right; SI Fig. 8). Although the mutation causes disappearance of the low-energy absorption band as well, the site energy shift of BChla 3 is much smaller (SI Table 6).

The electric field of  $\alpha$ -helical backbone segments has been proposed to play a significant role in the stabilization of protein structure and in protein function (see refs. 31–33). Recently, these effects were found to provide an important contribution to pigment redox potentials in photosynthetic reaction centers (20). Here, we have shown that in the FMO protein, the influence of  $\alpha$ -helices on the formation of an excitation energy funnel is dominant. As a consequence, point mutations will not be able to change the site energies enough to significantly alter the direction of energy flow. Regulating protein function in this way by means of the backbone architecture appears to be an intriguing

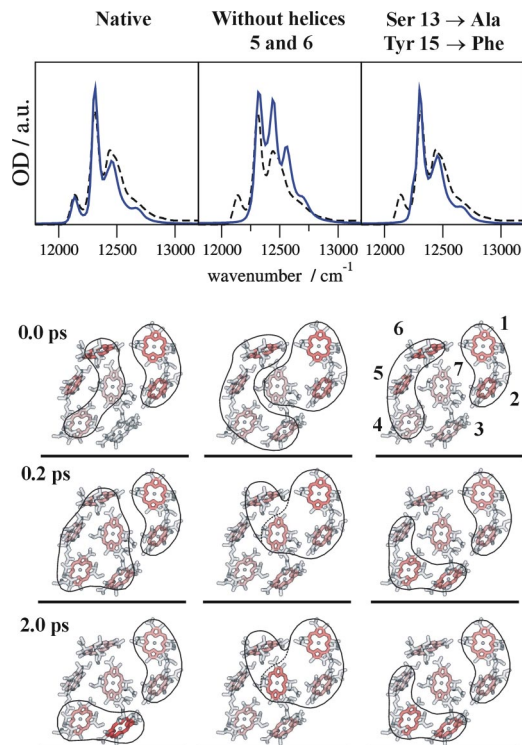


**Fig. 4.** Calculation of optical absorption spectra at 4 K (Upper, experimental wild-type spectra, dashed curves) and excitation energy transfer dynamics at 300 K (Lower) for the native FMO protein (Left); a system where the backbone partial charges of  $\alpha$ -helices 5 and 6 were set to zero (Center); and a simulated double mutation, where Ser-13 and Tyr-15 (see Fig. 3A) were replaced by Ala and Phe, respectively (Right). Orientation of pigments is the same as in Fig. 1C. The intensity of red in the pictorial representation of energy flow is proportional to the occupation probability,  $P_m(t)$ , of the local excited state of the respective pigment at a given time (0.0, 0.2, and 2.0 ps). The pigments that contribute to the two (delocalized) exciton states with the largest population,  $P_M(t)$ , at a given time are encircled (see SI for explicit time dependence of occupation probabilities).

possibility to establish robustness against mutations in the course of evolution.

We conclude that structure-based calculations of site energies in PPCs combining quantum chemistry and classical electrostatics are feasible with an uncertainty of  $\approx 60 \text{ cm}^{-1}$ , which is in the order of the optical line width at cryogenic temperatures. The method will serve as a starting point for the development of improved techniques, for example, incorporating protein dynamics and dispersive interactions. It helps to remove much of the ambiguity in the assignment of site energies and will contribute to a better understanding of biological and artificial chromophore arrays.

### Computational Procedures

Here, we give a brief summary of the computational procedures yielding site energies, excitonic couplings, optical spectra, and exciton relaxation rates. Further details can be found in the SI Text.

**Site Energies.** Our method for the determination of site energies comprises structure-based calculations of the free energy change of the PPC that occurs when the ground-state charge density of BChla  $m$  is changed to that of the first excited state. The calculations have two principle parts: One is a quantum chemical calculation of the pigments *in vacuo*, yielding charge distributions of the  $S_0$  and  $S_1$  states and a contribution  $\Delta X_{\text{qc}}^{(m)}$  to the  $S_0 \rightarrow$

$S_1$  transition energy originating from different orientations of the 3-acetyl group of the BChla in the various sites. The quantum chemical calculations are performed by using time-dependent density functional theory (B3LYP/6-31G\*) on a BChla model, where the phytyl chain is replaced by a methyl group and the 3-acetyl group retains the same orientation with respect to the tetrapyrrole macrocycle as in the x-ray crystallographic model (6).

The second part of the site energy calculation results in a contribution,  $\Delta X_{\text{elec}}^{(m)}$ , due to classical electrostatic interaction between the charge distributions of the  $S_0$  and  $S_1$  states with the protein environment. It corresponds to the shift of the  $S_0 \rightarrow S_1$  transition energy that is caused by transferring the pigment from a solvent into the protein with its given charge distribution (including the  $S_0$  charge distribution of the other pigments  $n \neq m$ ). We thus have for the site energy of BChla  $m$

$$X_m = X_0 + \Delta X_{\text{qc}}^{(m)} + \Delta X_{\text{elec}}^{(m)} \quad [1]$$

where  $X_0$  is a parameter that represents the transition energy of the pigment in the solvent. As was demonstrated recently (14), the Coulomb coupling between molecules can be described accurately and efficiently by interactions between atomic partial charges that are determined from a fit of the *ab initio* electrostatic potential of the respective electronic states of the molecules. Therefore,  $\Delta X_{\text{elec}}^{(m)}$  is calculated by means of classical electrostatics, where both protein and pigments are modeled by atomic partial charges embedded in a dielectric medium.

During excitation of BChla, the electrons but not the nuclei of the environment adapt to the newly established charge distribution of the pigment. This is a manifestation of the Franck-Condon principle. As a consequence, the protonation pattern of the protein stays relaxed with respect to the ground state of the pigments, and the excited state of BChla  $m$  interacts with a nonequilibrium polarization of the protein that is only electronically relaxed. We consider the nonequilibrium polarization in the classical electrostatic calculations by following the work of Marcus (21) and dividing  $\Delta X_{\text{elec}}^{(m)}$  into two parts:

$$\Delta X_{\text{elec}}^{(m)} = \Delta X_{\text{eq}}^{(m)} + \Delta X_{\text{corr}}^{(m)} \quad [2]$$

For the equilibrium contribution,  $\Delta X_{\text{eq}}^{(m)}$ , it is assumed that the charge distribution of the pigment in the excited state is in equilibrium with the total polarization of the environment (represented by the static dielectric constants  $\epsilon_{\text{protein}}$  and  $\epsilon_{\text{solvent}}$ ). Therefore, it can be determined by the same methods as used for the calculation of pigment redox potentials in PPCs (see refs. 20 and 34), which are based on the solution of the linearized Poisson-Boltzmann equation (35, 36) and a Monte Carlo procedure for the determination of protonation probabilities of titratable residues in the protein (18, 19). For the nonequilibrium correction term,  $\Delta X_{\text{corr}}^{(m)}$ , one has to consider the interaction of the charge density difference between the  $S_1$  and  $S_0$  states of the pigment with the surrounding dielectric (21). We find that this term makes only a small contribution to site energy differences (SI Table 1).

**Excitonic Couplings.** Excitonic couplings are calculated by combining the TrEsp method (14), in which the *ab initio* transition density of the  $S_0 \rightarrow S_1$  transition of BChla is represented by atomic partial charges, with the protein-adapted version of the transition monopole approximation (11) introduced in ref. 15, where the BChla molecules are represented as vacuum cavities in the dielectric volume of the protein with effective optical dielectric constant  $n^2 = 2.0$ . The TrEsp transition charges are scaled to yield a vacuum transition dipole magnitude of 6.1 Debye as determined by Knox and Spring (37). The different acetyl group orientations of the individual BChla molecules are

taken into account in the calculations of transition densities but do not significantly affect the excitonic couplings. For comparison, we show the results obtained with the point dipole approximation, which for the FMO protein is still adequate (SI Table 7, SI Fig. 9).

**Optical Spectra.** For the calculation of the linear absorption, circular dichroism, and linear dichroism spectra, the PPC is described by the Hamiltonian:

$$H_{\text{PPC}} = H_{\text{ex}} + H_{\text{ex-vib}} + H_{\text{vib}}. \quad [3]$$

Here,  $H_{\text{ex}}$  is the Hamiltonian of electronic states of the chromophore system,  $H_{\text{vib}}$  is the Hamiltonian of molecular vibrations of the PPC, and  $H_{\text{ex-vib}}$  represents exciton–vibrational coupling.  $H_{\text{vib}}$  is approximated by a set of effective harmonic oscillators that do not change their frequencies on electronic excitation of the pigments.  $H_{\text{ex-vib}}$  contains the modulation of pigment transition energies that depends linearly on the displacements of the harmonic oscillators from their equilibrium positions in the electronic ground state. The electron–vibrational coupling constants are contained in the spectral density  $J(\omega)$  that is assumed to be site-independent and determines the shape of vibrational side bands and the rate constants of exciton relaxation. The explicit form of  $J(\omega)$  was deduced in earlier work (9) from fluorescence line-narrowing spectra and the temperature dependence of the absorption spectrum (15) and yields a reorganization energy for the  $S_0 \rightarrow S_1$  transition of BChla in the FMO protein of  $E_\lambda = 40 \text{ cm}^{-1}$ . In the basis of localized excited states  $|m\rangle$ , in which one pigment is in the  $S_1$  state and all others are in the  $S_0$  state, the  $X_m$  calculated from Eq. 1 are the diagonal elements of  $H_{\text{ex}}$ , and the excitonic couplings  $V_{mn}$  are the off-diagonal elements. The diagonalization of  $H_{\text{ex}}$  yields the energies,  $E_M$ , and coefficients,  $c_m^{(M)}$ , of the delocalized exciton states,  $|M\rangle$ , which are linear combinations of the local excited states,  $|m\rangle$ . The intensities and positions of optical bands observed in the absorption spectrum are determined by the square of the exciton transition dipole moments

$$\mu_M = \sum_m c_m^{(M)} \mu_m \quad [4]$$

and the exciton energies,  $E_M$ , respectively. The orientations of the local transition dipoles  $\mu_m$  are determined from the atomic partial charges (TrEsp method) assigned to atomic coordinates of the crystal structure (6). They all lie within  $\pm 2^\circ$  of the  $N_B$ – $N_D$

axis used in earlier work to define the orientation of the  $Q_Y$  transition (15).

In the basis of delocalized states  $|M\rangle$ ,  $H_{\text{ex-vib}}$  has diagonal elements ( $M = N$ ) and off-diagonal elements ( $M \neq N$ ) giving rise to vibrational side bands and lifetime broadening of the exciton transitions, respectively. These effects are described by the homogeneous absorption line-shape function,  $D_M(\omega)$ , which is a function of  $E_M$ ,  $c_m^{(M)}$ , and  $J(\omega)$  (9). Inhomogeneous broadening is simulated by a Monte Carlo procedure, in which each value of  $X_m$  is taken as the center of a Gaussian distribution,  $F_m$ , and the site energies are varied independently of each other. For each set of randomly generated site energies,  $H_{\text{ex}}$  is diagonalized and the resulting homogeneous absorption, circular dichroism, and linear dichroism spectra are each averaged. The same disorder average is used in the calculation of exciton relaxation described below.

The strongest excitonic coupling between two BChla molecules in different FMO monomers is about an order of magnitude smaller than the local reorganization energy,  $E_\lambda$ . Therefore, the coherence between the excited states of these pigments is destroyed by vibrational dynamics. We include this dynamical localization implicitly by assuming that delocalized states can be formed only between pigments of the same FMO monomer, that is, we set the intermonomer excitonic couplings to zero.

**Exciton Relaxation.** For calculations of exciton relaxation, multi-level Redfield theory is used and a master equation is solved for the populations,  $P_M(t)$ , of exciton states (15). The initial populations,  $P_M(0)$ , are determined by the exciton coefficients of pigments 1 and 6 in the different states  $|M\rangle$ , as well as the overlap integral of the homogeneous absorption line-shape function,  $D_M(\omega)$ , and the homogeneous fluorescence line-shape function of the baseplate,  $D^{(f)}(\omega)$ . The function  $D^{(f)}(\omega)$  is extracted from experimental spectra of *Chloroflexus aurantiacus* (S. Lin and G. Montaño, personal communication), because it is the only species from which the baseplate has been isolated so far (38). Although *C. aurantiacus* lacks the FMO protein, its baseplate absorption and fluorescence are very similar to those of *P. aestuarii* (R. E. Blankenship, personal communication) and other green sulfur bacteria (39).

We thank D. Bashford and M. Karplus for providing the programs MEAD and CHARMM; Y. Shao and S. T. Brown for incorporating the possibility to calculate excited-state electrostatic potentials into *Q-Chem*; G. Kieseritzky, V. May, and A. Zouni for insightful discussions; S. Lin and G. Montaño for sending us baseplate fluorescence data; and R. E. Blankenship for helpful comments concerning the optical properties of green bacteria. This work was supported by Deutsche Forschungsgemeinschaft through Emmy-Noether Grant RE16-10.

- Green BR, Parson WW (2003) *Light-Harvesting Antennas in Photosynthesis* (Kluwer, Dordrecht, The Netherlands).
- Wendling M, Przyjalowski MA, Gülen D, Vulto SIE, Aartsma TJ, van Grondelle R, van Amerongen H (2002) *Photosynth Res* 71:99–123.
- Brixner T, Stenger J, Vaswani HM, Cho M, Blankenship RE, Fleming GR (2005) *Nature* 434:625–628.
- Engel GS, Calhoun TR, Read EL, Ahn TK, Mančal T, Cheng YC, Blankenship RE, Fleming GR (2007) *Nature* 446:782–786.
- Fenna RE, Matthews BW (1975) *Nature* 258:573–577.
- Tronrud DE, Schmid MF, Matthews BW (1986) *J Mol Biol* 188:443–454.
- Li YF, Zhou W, Blankenship RE, Allen JP (1997) *J Mol Biol* 271:456–471.
- Renger T, May V, Kühn O (2001) *Phys Rep* 343:137–254.
- Renger T, Marcus RA (2002) *J Chem Phys* 116:9997–10019.
- Pearlstein RM (1991) in *Chlorophylls*, ed Scheer H (CRC, Boca Raton, FL), pp 1048–1078.
- Chang JC (1977) *J Chem Phys* 67:3901–3909.
- Warshel A, Parson WW (1987) *J Am Chem Soc* 109:6143–6152.
- Krueger BP, Scholes GD, Fleming GR (1998) *J Phys Chem B* 102:5378–5386.
- Madjet ME, Abdurahman A, Renger T (2006) *J Phys Chem B* 110:17268–17281.
- Adolphs J, Renger T (2006) *Biophys J* 91:2778–2797.
- Gudowska-Nowak E, Newton MD, Fajer J (1990) *J Phys Chem* 94:5795–5801.
- Damjanovic A, Vaswani HM, Fromme P, Fleming GR (2002) *J Phys Chem B* 106:10251–10262.
- Rabenstein B (1999) KARLSBERG, A Monte Carlo pH and Redox Titration of Proteins Program (Free University of Berlin, Berlin).
- Rabenstein B, Knapp EW (2001) *Biophys J* 80:1141–1150.
- Ishikita H, Saenger W, Biesiadka J, Loll B, Knapp EW (2006) *Proc Natl Acad Sci USA* 103:9855–9860.
- Marcus RA (1963) *J Chem Phys* 38:1858–1862.
- Blankenship RE, Olson JM (1995) in *Anoxygenic Photosynthetic Bacteria*, eds Blankenship RE, Madigan MT, Bauer CE (Kluwer, Dordrecht, The Netherlands), pp 399–435.
- Li H, Frigaard NU, Bryant DA (2006) *Biochemistry* 45:9095–9103.
- Egawa A, Fujiwara T, Mizoguchi T, Kakitani Y, Koyama Y, Akutsu H (2007) *Proc Natl Acad Sci USA* 104:790–795.
- Melkozernov AN, Olson JM, Li YF, Allen JP, Blankenship RE (1998) *Photosynth Res* 56:315–328.
- Rémigy HW, Stahlberg H, Fotiadis D, Müller SA, Wolpensinger B, Engel A, Hauska G, Tsotis G (1999) *J Mol Biol* 290:851–858.
- Louwe RJW, Vrieze J, Hoff AJ, Aartsma TJ (1997) *J Phys Chem B* 101:11280–11287.
- Eccles J, Honig B (1983) *Proc Natl Acad Sci USA* 80:4959–4962.
- Fowler GJS, Visschers RW, Grief GG, van Grondelle R, Hunter CN (1992) *Nature* 355:848–850.

30. Yu IS (1993) *Meas Sci Technol* 4:344–348.
31. Sheridan RP, Levy RM, Salemm FR (1982) *Proc Natl Acad Sci USA* 79:4545–4549.
32. Hol WGL (1985) *Prog Biophys Mol Biol* 45:149–195.
33. Sitkoff D, Lockhart DJ, Sharp KA, Honig B (1994) *Biophys J* 67:2251–2260.
34. Ullmann GM, Knapp EW (1999) *Eur Biophys J* 28:533–551.
35. Bashford D, Karplus M (1990) *Biochemistry* 29:10219–10225.
36. Bashford D, Case DA, Dalvit C, Tennant L, Wright PE (1993) *Biochemistry* 32:8045–8056.
37. Knox RS, Spring BQ (2003) *Photochem Photobiol* 77:497–501.
38. Montaña GA, Wu HM, Lin S, Brune DC, Blankenship RE (2003) *Biochemistry* 42:10246–10251.
39. Causgrove TP, Brune DC, Blankenship RE (1992) *J Photochem Photobiol B: Biol* 15:171–179.